

VLT/X-shooter spectroscopy of the GRB 090926A afterglow [★]

V. D'Elia^{1,2}, J. P. U. Fynbo³, S. Covino⁴, P. Goldoni^{5,6}, P. Jakobsson⁷, F. Matteucci⁸, S. Piranomonte¹, J. Sollerman^{3,9}, C.C. Thöne⁴, S.D. Vergani^{10,11}, P.M. Vreeswijk³, D.J. Watson³, K. Wiersema¹², T. Zafar³, A. de Ugarte Postigo⁴, H. Flores¹¹, J. Hjorth³, L. Kaper¹³, A.J. Levan¹⁴, D. Malesani³, B. Milvang-Jensen³, E. Pian^{8,15}, G. Tagliaferri⁴, N.R. Tanvir¹²

¹INAF-Osservatorio Astronomico di Roma, Via Frascati 33, I-00040 Monteporzio Catone, Italy

²ASI-Science Data Centre, Via Galileo Galilei, I-00044 Frascati, Italy

³Dark Cosmology Centre, Niels Bohr Institute, University of Copenhagen, Juliane Maries Vej 30, 2100 Copenhagen, Denmark

⁴INAF-Osservatorio Astronomico di Brera, via E. Bianchi 46, 23807 Merate (LC), Italy

⁵Laboratoire Astroparticule et Cosmologie, 10 rue A. Domon et L. Duquet, 75205 Paris Cedex 13, France

⁶DSM/IRFU/Service D'Astrophysique, CEA-Saclay, 91191 Gif-sur-Yvette, France

⁷Centre for Astrophysics and Cosmology, Science Institute, University of Iceland, Dunhagi 5, 107 Reykjavik, Iceland

⁸INAF, Osservatorio Astronomico di Trieste, Via Tiepolo 11, 34143 Trieste, Italy

⁹The Oskar Klein Centre, Department of Astronomy, AlbaNova, Stockholm University, 106 91 Stockholm, Sweden

¹⁰University Paris 7, APC, Lab. Astroparticule et Cosmologie, UMR7164 CNRS, 10 rue Alice Domon et Lonie Duquet 75205 Paris Cedex 13, France

¹¹Laboratoire Galaxies Etoiles Physique et Instrumentation, Observatoire de Paris, 5 place Jules Janssen, 92195 Meudon, France

¹²Department of Physics and Astronomy, University of Leicester, Leicester LE1 7RH, UK

¹³Astronomical Institute "Anton Pannekoek", University of Amsterdam, Science Park 904, 1098 XH Amsterdam, The Netherlands

¹⁴Department of Physics, University of Warwick, Coventry, CV4 7AL, UK

¹⁵Scuola Normale Superiore, Piazza dei Cavalieri 7, 56126, Pisa, Italy;

Preprint online version: December 12, 2021

ABSTRACT

Aims. The aim of this paper is to study the environment and intervening absorbers of the gamma-ray burst GRB 090926A through analysis of optical spectra of its afterglow.

Methods. We analyze medium resolution spectroscopic observations ($R = 10000$, corresponding to 30 km s^{-1} , $S/N = 15 - 30$ and wavelength range $3000 - 25000$) of the optical afterglow of GRB 090926A, taken with X-shooter at the VLT ~ 22 hr after the GRB trigger.

Results. The spectrum shows that the ISM in the GRB host galaxy at $z = 2.1071$ is rich in absorption features, with two components contributing to the line profiles. In addition to the ground state lines, we detect C II, O I, Si II, Fe II and Ni II excited absorption features. No host galaxy emission lines, molecular absorption features nor diffuse interstellar bands are detected in the spectrum. The line of sight of GRB 090926A presents four weak intervening absorption systems in the redshift range $1.24 < z < 1.95$.

Conclusions. The Hydrogen column density associated to GRB 090926A is $\log N_{\text{H}}/\text{cm}^{-2} = 21.60 \pm 0.07$, and the metallicity of the host galaxy is in the range $[X/H] = 3.2 \times 10^{-3} - 1.2 \times 10^{-2}$ with respect to the solar values, i.e., among the lowest values ever observed for a GRB host galaxy. A comparison with galactic chemical evolution models has suggested that the host of GRB090926A is likely to be a dwarf irregular galaxy. No emission lines were detected, but we note that a $H\alpha$ flux in emission of $9 \times 10^{-18} \text{ erg s}^{-1} \text{ cm}^{-2}$ (i.e., a star formation rate of $2 M_{\odot} \text{ yr}^{-1}$), which is typical of many GRB hosts, would have been detected in our spectra, and thus emission lines are well within the reach of X-shooter. We put an upper limit to the H molecular fraction of the host galaxy ISM, which is $f < 7 \times 10^{-7}$. The continuum has been fitted assuming a power-law spectrum, with a spectral index of $\beta = 0.89^{+0.02}_{-0.02}$. The best fit does not essentially require any intrinsic extinction since $E_{B-V} < 0.01$ mag adopting a SMC extinction curve.

We derive information on the distance between the host absorbing gas and the site of the GRB explosion. The distance of component I is found to be 2.40 ± 0.15 kpc, while component II is located far away from the GRB, possibly at ~ 5 kpc. These values are compatible with that found for other GRBs.

Key words. gamma rays: bursts - cosmology: observations - galaxies: abundances - ISM

1. Introduction

The study of the inter stellar medium (ISM) of $z \geq 1$ galaxies has traditionally relied upon Lyman-break galaxies (LBGs) at $z = 3 - 4$ (see e.g. Steidel et al. 1999), K-band selected galaxies

(Savaglio et al. 2004) and galaxies which happen to be along the lines of sight to bright background quasars (or QSOs). However, LBGs are characterized by pronounced star-formation and their inferred chemical abundances may relate to these regions rather than being representative of typical high-redshift galaxies. Weak metal line systems along the line of sight to quasars probe mainly galaxy haloes, rather than their bulges or discs (Fynbo et al. 2008). Taking advantage of ultra-deep Gemini multi-object

* Based on observations collected at the European Southern Observatory, ESO, the VLT/Kueyen telescope, Paranal, Chile, during the science verification phase, proposal code: 060-9427(A).

spectrograph observations, Savaglio et al. (2004, 2005) studied the ISM of a sample of faint K -band selected galaxies at $1.4 < z < 2.0$, finding MgII and FeII abundances much higher than in QSO systems but similar to those in GRB host galaxies. Such studies can hardly be extended to higher redshift with the present generation of 8m class telescopes, because of the faintness of high-redshift galaxies. Since the discovery that gamma-ray bursts (GRBs) are extragalactic, we now can avail of an independent tool to study the ISM of high-redshift galaxies.

Metallicities measured in GRB host galaxies vary from less than 10^{-2} to nearly solar values and are on average larger than those found along QSO sightlines (see e.g., Fynbo et al. 2006, Prochaska et al. 2007). This result supports the notion that GRBs originate in dwarf and/or low-mass galaxies. Since star formation occurs in molecular clouds, the latter are expected to be the GRB birthplaces. In this scenario, absorption from ground-state and vibrationally excited levels of the H_2 molecules are expected, but these are typically not observed in GRB afterglow spectra (Vreeswijk et al. 2004, Tumlinson et al. 2007). The non-detection of H_2 molecules (with the exception of GRB 080607, see Prochaska et al. 2009, Sheffer et al. 2009) can possibly be explained by photo-dissociation by the intense UV flux from the GRB afterglow.

Indeed, the main difference between QSO and GRB absorption spectroscopy is that QSOs are nearly stationary in their emission, while GRBs are the most variable and violent phenomena in the Universe. Thus, while QSOs have the time to ionize the ISM along their lines of sight, the physical, dynamical and chemical status of the circumburst medium in the star-forming region hosting GRB progenitors can be modified by the explosive event, through shock waves and ionizing photons. The transient nature of GRBs is manifested through the detection of fine structure and other excited levels of the atom O I and the ions Fe II, Ni II, Si II and C II. These features are routinely identified in GRB spectra, and are most probably excited by the intense UV flux from the afterglow, since strong variation is observed when multi-epoch spectroscopy is available. This variation is not consistent with a pure infrared excitation or collisional processes (Prochaska, Chen & Bloom 2006, Vreeswijk et al. 2007, D'Elia et al. 2009a). Thus, assuming UV pumping as the responsible mechanism for the production of these lines, the distance of the gas to the GRB can be computed. This distance comes out to be of the order of a few hundred pc (see D'Elia et al. 2009b for GRB 080330 and Ledoux et al. 2009 for GRB 050730) or even in the kpc scale (see Vreeswijk et al. 2007 for GRB 060418 and D'Elia et al. 2009a for the naked-eye GRB 080319B).

GRB spectroscopy is also suitable for studying systems lying along the line of sight to GRBs. Surprisingly, the number density of strong Mg II intervening absorbers in GRB spectra is more than twice larger than along QSO sightlines (Prochter et al. 2006, Vergani et al. 2009), while C IV absorbers do not show any statistical difference (Sudilovsky et al. 2007, Tejos et al. 2007). The reason for the Mg II excess in GRB spectra is still unclear, and a larger sample is needed to properly address this issue (Porciani et al. 2007, Cucchiara et al. 2009).

All these issues can now be systematically addressed using the X-shooter spectrograph. This is the first second-generation instrument at the ESO's Very Large Telescope (VLT) at Paranal Observatory (Chile). It is a single target spectrograph capable of obtaining a medium resolution spectrum ($R = \lambda/\Delta\lambda = 4000 - 14,000$) covering the spectral range 3000 - 24,800 Å in a single exposure thanks to the splitting of the light into three arms: ultraviolet/blue (UVB), visual (VIS) and near-infrared (NIR). The high spectrograph efficiency allowed us to obtain good quality

observations of the GRB 090313 afterglow (de Ugarte Postigo et al. 2010), although it being observed two days after the burst and under unfavourable conditions. We refer the reader to D'Odorico et al. (2006) for a more complete description of the X-shooter specifications and capabilities.

We discuss here the case of GRB 090926A, observed by X-shooter the 27th of September 2009. We investigate both the local medium surrounding the GRB, and the intervening systems. We derive the metallicity by comparing the column densities of Hydrogen and metals, we search for molecular absorption and galactic emission lines, and we constrain the distance between the GRB and the absorber by comparing the ratios between the ground and excited level column densities with photoexcitation codes, under the assumption of indirect UV pumping production of the excited levels. An analysis of the intervening absorbers lying along the line of sight to the GRB afterglow and a search for diffuse interstellar bands (DIBs) is also presented.

The paper is organized as follows. Section 2 makes a short summary of the GRB 090926A detection and observations from the literature; Section 3 presents the X-shooter observations and data reduction; Sections 4 and 5 are devoted to the study of the features from the host galaxy, Sect. 6 derives the extinction curve shape for this GRB; Section 7 presents the analysis of the other absorbing systems identified in the GRB 090926A line of sight; finally in Sect. 8 the results are discussed and conclusions are drawn. We assume a cosmology with $H_0 = 70 \text{ km s}^{-1} \text{ Mpc}^{-1}$, $\Omega_m = 0.3$, $\Omega_\Lambda = 0.7$. Hereafter, the $[\]$ refers to element abundances relative to Solar values and X refers to any chemical element.

2. GRB 090926A

GRB 090926A was discovered by *Fermi* on September 26, 2009, at 04:20:26 UT, and was detected by both the GBM (Bissaldi 2009) and the LAT (Uehara et al. 2009) instruments. *Swift* re-pointed to the target 13 hr later and found the X-ray counterpart (Vetere et al. 2009). The afterglow was later reported to be detected at optical wavelengths with the Skynet/PROMPT telescopes (Haislip et al. 2009) and with UVOT (Gronwall & Vetere 2009); the reported PROMPT magnitude was $R \sim 18$, although the observations took place almost 20 hr post burst. The redshift was secured by X-shooter, which observed the afterglow 2 hr after these optical detections. The preliminary reported value was $z = 2.1062$ (Malesani et al. 2009). FORS2 spectroscopic observations and GROND photometric follow-up of the GRB 090926A afterglow have been presented in Rau et al. (2010, hereafter R10): we will compare our results with those of R10 in the following.

Table 1. X-shooter observations

Observation	Time since burst (hr)	Exposure (s)	S/N
1	22.13	600	5 - 15
2	22.29	600	5 - 15
3	22.51	600	5 - 15
4	22.68	600	5 - 15
1+2+3+4	22.37	2400	10 - 30

3. Observations and data reduction

In the framework of the Science Verification phase program, we observed the afterglow of GRB 090926A with X-shooter

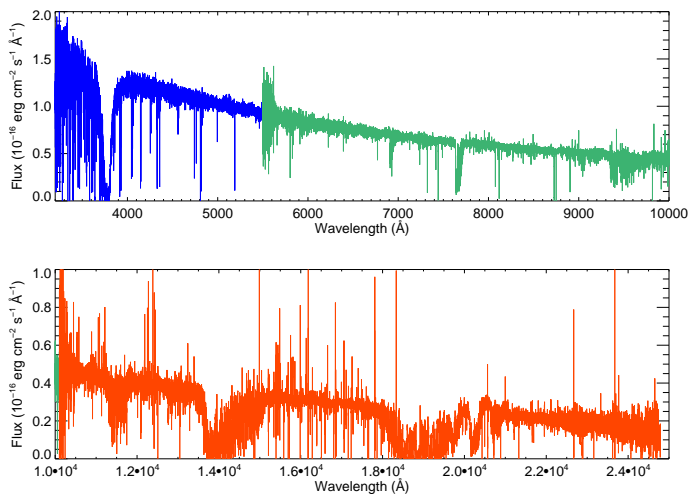


Fig. 1. The flux-calibrated X-shooter spectrum of GRB 090926A. Top: ultraviolet/blue and visual arms. Bottom: near-infrared arm. The absolute flux calibration may be not accurate due to slit losses.

(D’Odorico et al. 2006), mounted at the VLT-UT2 telescope. The observations consist of 4 different exposures of 600 s each (see Table 1). The exposures were taken using the nodding along the slit technique with an offset of 5 arcsec between exposures in a standard ABBA sequence. The sequence began on September 27th, 2007 at 02:23:14 UT, ~ 22 hr after the GRB trigger. The magnitude of the afterglow at the time of the observation was reported by R10 to be $R = 18.7$, which translates into a 6600\AA flux of $0.8 \times 10^{-16} \text{ erg cm}^{-2} \text{ s}^{-1} \text{ \AA}^{-1}$. The total net exposure time of our observations is 40 min. The slit width was set to $0.9''$ in the VIS and NIR arms and $1.0''$ in the UVB arm. The UVB and VIS CCD detectors were rebinned to 1×2 pixels (binned in the spectral direction but not in the spatial one) to reduce the readout noise.

We processed the spectra using a preliminary version of the X-shooter data reduction pipeline (Goldoni et al. 2006). The pipeline performed the following actions: The raw frames were first bias subtracted and cosmic ray hits were detected and removed using the method developed by van Dokkum (2001). The orders were extracted and rectified in wavelength space using a wavelength solution previously obtained from calibration frames. The resulting rectified orders were shifted and coadded to obtain the final 2D spectrum. In the overlapping regions, orders were merged by weighting them according to the errors propagated during the entire reduction process. From the resulting 2D merged spectrum, a one dimensional spectrum was extracted at the source position. The one dimensional spectrum with the corresponding error file and bad pixel map is the final product of the reduction.

The resolution is $R \sim 10,000$ and the achieved spectral range is ~ 3000 to $\sim 24,800 \text{ \AA}$. The data below ~ 3020 and above $\sim 24,000 \text{ \AA}$ are, however, totally dominated by noise. To perform flux calibration we extracted a spectrum from a staring observation of the flux standard BD +17deg4708 (Bohlin & Gilliland 2004). In this case we subtracted the sky emission lines using the Kelson (2003) method. This spectrum was divided by the flux table of the same star from the CALSPEC HST database (Bohlin 2007, <http://www.stsci.edu/hst/observatory/cdbs/calspec.html>) to produce the response function. The response was then interpolated

where needed in the atmospheric absorption bands in VIS and NIR and applied to the spectrum of the source. No telluric correction was applied, so that prominent atmospheric bands, especially in the NIR arm, can still be seen (Fig. 1). We searched for variability in the absorption features, but we found none (the equivalent widths in the four spectra are constant at the 1.5σ level), so we summed the four, flux-calibrated observations (see Fig. 1). This lack of variability is not surprising, since the spectra have been acquired nearly 1 day after the burst (see Sect. 4.3 for details). The signal-to noise ratio (per pixel) ranges from ~ 10 to ~ 30 in the co-added spectrum. In order to perform line fitting (see section 4) the spectrum was normalized to the continuum, which was evaluated by fitting the data with cubic splines, after the removal of the absorption features. Finally, the noise spectrum, used to determine the errors on the best fit line parameters, was calculated from the real, background-subtracted spectrum using line-free regions. This takes into account both statistical and systematic errors in the pipeline processing and background subtraction.

4. The host galaxy atomic absorption features

The gas residing in the GRB host galaxy is responsible for many of the features observed in the GRB 090926A afterglow spectrum. Metallic features are apparent, from neutral (OI, Mg I, Ca I), low ionization (C II, Mg II, Al II, Al III, Si II, S II, Ca II, Fe II, Ni II) and high ionization (C IV, N V, O VI, Si IV, S IV) species. In addition, strong absorption from the fine structure levels of C II, O I, Si II, Fe II and from the metastable level of Ni II is identified, suggesting that the intense radiation field from the GRB excites such features. Table 2 gives a summary of all the absorption lines due to the host galaxy gas. The analysis of the spectral features has been performed with FITLYMAN (Fontana & Ballester 1995). This program is able to simultaneously fit several absorption lines, linking the redshifts, column densities and Doppler parameters if required. FITLYMAN takes into account the atomic masses when a thermal model of the Doppler broadening is adopted (as we did), enabling to link the Doppler parameters of different species. The probed ISM of the host galaxy is resolved into two components separated by 48 km s^{-1} which contribute to the absorption system. The wealth of metal-line transitions allows us to precisely determine the redshift of the GRB host galaxy. This yields a vacuum-heliocentric value of $z = 2.1071 \pm 0.0001$, setting the reference point to the red component of the main system; this component is the only one for which there is significant absorption from all the excited levels of the intervening gas (see Sect. 4.1 and 4.3). This redshift value supersedes that reported by Malesani et al. (2009), which was based on archival calibration data and using an older X-shooter pipeline version. The host galaxy environment will be described in the next sub-sections together with a study of the excited lines aimed at estimating the distance from the GRB of the circumburst gas.

4.1. Line fitting procedure

In general, the analysis of the GRB environment is not straightforward due to the complexity of the absorption lines profile, which in several cases cannot be fitted with a single line profile. This means that many components contribute to the gas in the GRB environment. In other words, several layers of gas which may be close to or far from each other, appear mixed together in the spectrum (in velocity space). The presence of several components is thus indicative of clumpy gas in the GRB environ-

ment, composed of different absorbing regions each with different physical properties. This behaviour is particularly evident for GRB afterglows observed at high resolution (see e.g. Fiore et al. 2005, Thöne et al. 2008).

For what concerns GRB 090926A, the CIV and Si IV lines have the wider velocity range. This behaviour is common to many GRBs (see e.g. D'Elia et al. 2007, Piranomonte et al. 2008), where these lines are the ones that are most clearly detected and used to guide the identification of the different components constituting the circumburst matter. A two-component model provides a good fit for the CIV and Si IV lines (Fig. 2). Thus, the redshifts and the Doppler parameters of these components were fixed in order to fit the other species present in the spectrum with the same model. This modeling adequately fits all other absorption lines at the GRB redshift. All species feature absorption in the red component, and most of them have absorption also in the blue component. Figures 3 and 4 show the two-component model fit to all the absorption lines at the GRB redshift. Asterisks mark the fine structure levels. The lines Ni II $\lambda\lambda 2166, 2217$ and 2316 (Fig. 4, left) are produced by the Ni II second excited level ($^4F_{9/2}$). The Si III blue component could not be derived because of blending with Ly α forest features (Fig. 4, right).

The column densities for all the elements and ions of the host galaxy absorbing gas, estimated using this two-component model, are reported in Table 2. The upper limits reported are at the 90% confidence level. The red and blue components are marked as I and II, respectively. The reference zero point of the velocity shifts has been placed at $z = 2.1071$, coincident with the redshift of the red component. Component I of Al III needs a slight wavelength red-shift in order to be adequately fitted (Fig. 3, bottom left). Anyway, the resulting column density of this component is consistent with the value obtained linking the Al III and CIV central wavelengths. The features of some species, such as Mg II, O I, O VI and C II, could be saturated at least in component I. In this case, the column densities in Table 2 should be regarded as lower limits to the real values. The column density of Si II has been calculated using the $\lambda 1304$ transition only (see Sect. 4.3). It is interesting to note that among the excited absorption features in the spectrum, produced by fine structure and/or metastable levels, C II, Si II and Ni II show significant absorption in both components I and II (the absorption in component II from Ni II is marginal), while O I and Fe II only show this in the red, reference component I. We fixed the zero point to the redshift of component I because the Fe II fine structure levels require a high UV flux in order to remain populated (see Sect. 4.3), implying that component I is possibly closer to the GRB explosion site than II. As described in the introduction, the observation of excited states in GRB absorption spectra is a quite common feature. Sub-section 4.3 is thus devoted to these features and to the information that can be extracted from their analysis.

4.2. Metallicities

The GRB 090926A redshift was high enough to allow the Hydrogen Ly α and Ly β lines to enter the X-shooter spectral window. Ly α can be clearly seen in Fig. 1 (upper panel) at ~ 4000 Å. We used the two Lyman features in order to constrain the Hydrogen column density. Figure 5 shows the Lyman- α and Lyman- β profiles. Both features are damped and we can not separate the two components identified in the metal-line fits. The Hydrogen column density computed has $\log(N_{\text{H}}/\text{cm}^{-2}) =$

Table 2. Absorption line column densities for the two components of the main system.

Species	Observed transitions	I (0 km s ⁻¹)	II (-48 km s ⁻¹)
HI $^2S_{1/2}$	Ly α , Ly β	21.60 \pm 0.07	-
CII $^2P_{1/2}^0$	$\lambda 1036, \lambda 1334$	14.48 \pm 0.04	14.04 \pm 0.04
CII $^2P_{3/2}^0$	$\lambda 1037, \lambda 1335$	> 14.45 \pm 0.04	14.01 \pm 0.05
CIV $^2S_{1/2}$	$\lambda 1548, \lambda 1550$	14.43 \pm 0.02	13.89 \pm 0.03
NV $^2S_{1/2}$	$\lambda 1238, \lambda 1242$	14.08 \pm 0.03	13.66 \pm 0.07
OI 3P_2	$\lambda 1039, \lambda 1302$	> 14.75 \pm 0.03	< 13.8
OI 3P_1	$\lambda 1304$	14.49 \pm 0.03	< 13.7
OI 3P_0	$\lambda 1306$	14.37 \pm 0.04	< 13.7
OVI $^2S_{1/2}$	$\lambda 1031, \lambda 1037$	> 14.60 \pm 0.16	Blend
MgI 1S_0	$\lambda 2852$	12.74 \pm 0.01	11.98 \pm 0.05
MgII $^2S_{1/2}$	$\lambda 1239, \lambda 1240$ $\lambda 2796, \lambda 2803$	> 14.05 \pm 0.01	13.05 \pm 0.02
AlII 1S_0	$\lambda 1670$	13.20 \pm 0.03	12.66 \pm 0.04
AlIII $^2S_{1/2}$	$\lambda 1854, \lambda 1862$	13.24 \pm 0.03	< 12.3
SiII $^2P_{1/2}^0$	$\lambda 1020, \lambda 1190$ $\lambda 1193, \lambda 1260$ $\lambda 1304, \lambda 1526$ $\lambda 1808$	14.41 \pm 0.03	13.98 \pm 0.07
SiII $^2P_{3/2}^0$	$\lambda 1194, \lambda 1197$ $\lambda 1264, \lambda 1309$ $\lambda 1533, \lambda 1309$	13.96 \pm 0.03	13.42 \pm 0.09
SiIII 1S_0	$\lambda 1206$	13.50 \pm 0.11	Blend
SiIV $^2S_{1/2}$	$\lambda 1393, \lambda 1402$	13.97 \pm 0.03	13.61 \pm 0.04
SII $^4S_{3/2}^0$	$\lambda 1250, \lambda 1253$ $\lambda 1259$	14.89 \pm 0.06	< 14.3
SIV $^4S_{3/2}^0$	$\lambda 1062, \lambda 1253$	14.45 \pm 0.19	< 14.2
CaI 1S_0	$\lambda 4227$	12.15 \pm 0.07	< 11.9
CaII $^2S_{1/2}$	$\lambda 3969$	13.21 \pm 0.03	< 12.8
MnII a^7S_3	$\lambda 2576$	< 12.3	< 12.3
FeII $a^6D_{9/2}$	$\lambda 1081, \lambda 1096$ $\lambda 1144, \lambda 2344$ $\lambda 2348, \lambda 2374$ $\lambda 2382, \lambda 2586$ $\lambda 2600$	14.03 \pm 0.03	13.46 \pm 0.04
FeII $a^6D_{7/2}$	$\lambda 2333, \lambda 2396$ $\lambda 2612, \lambda 2626$	12.52 \pm 0.08	< 12.2
FeII $a^4F_{9/2}$	$\lambda 1559, \lambda 2332$	< 13.6	< 13.6
FeIII 5D_4	$\lambda 1122$	14.54 \pm 0.07	14.38 \pm 0.10
NiII $^2D_{5/2}$	$\lambda 1317, \lambda 1370$ $\lambda 1454, \lambda 1703$ $\lambda 1709, \lambda 1741$ $\lambda 1751$	13.51 \pm 0.06	13.09 \pm 0.30
NiII $^4F_{9/2}$	$\lambda 2166, \lambda 2217$ $\lambda 2316$	13.54 \pm 0.02	12.47 \pm 0.36

All values of the column densities are logarithmic (in cm⁻²). Reported lower limits are due to possible line saturation.

21.60 \pm 0.07 cm⁻², for a reduced χ^2 value of 1.33, and is virtually insensitive to the adopted b parameter. From this N_{H} value, we can compute the metallicity for the host of GRB 090926A, using the metallic column densities reported in Table 2. Due to the wide spectral coverage of X-shooter, this can be done for a large number of elements. We proceeded as follows: first of all, since the Lyman features cannot be resolved into components, we summed up line by line the values in table 2 (e.g., the two components) to obtain the total column density for each species; second, we summed the total column densities of the transitions belonging to the same atom (different ionization and excitation states), in order to evaluate the atomic column densities. These values have been divided by N_{H} , and compared to the corresponding solar values given in Asplund et al. (2009). The results

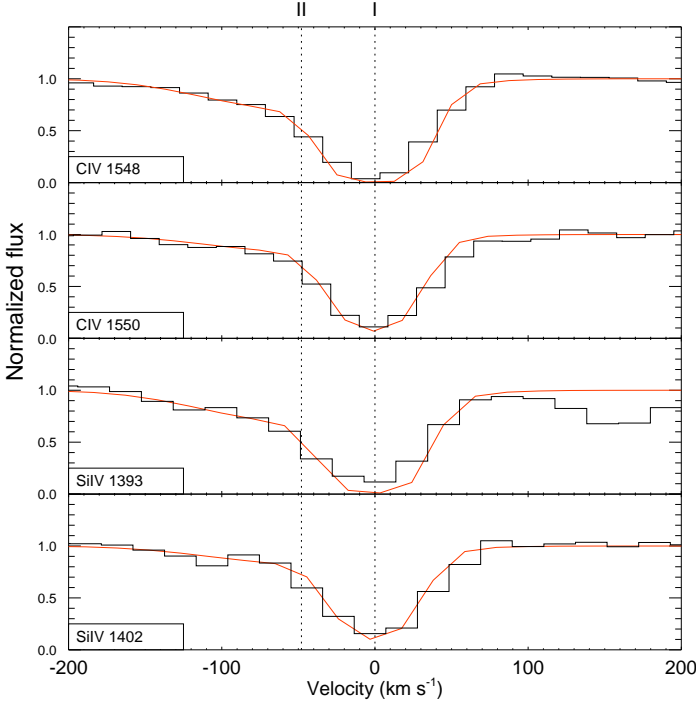


Fig. 2. The CIV and SiIV absorption features. Solid lines represent the two Voigt components, best fit model. Vertical lines identify the component velocities. The zero point has been arbitrarily placed at the redshift of the red component ($z = 2.1071$).

are listed in Table 3. Column 2 reports the total abundance of each atom, while columns 3 and 4 report the absolute and solar-scaled N_X/N_H ratios, respectively, with X being the corresponding element in column 1. Lower limits are reported whenever saturation does not allow us to securely fit the metallic column densities. We derive very low metallicity values with respect to the solar ones, between 4.2×10^{-3} and 1.4×10^{-2} . The very low value derived for N is due to the fact that we could not fit low ionization lines, but the N V species only, meaning that this value is not truly representative for all the N ionization states.

Table 3. Metallicities

Element X	$\log N_X/\text{cm}^{-2}$	$\log N_X/N_H$	$[X/H]$
C	$> 15.05 \pm 0.10$	$> -6.55 \pm 0.10$	$> -2.94 \pm 0.10$
N	14.22 ± 0.08	-7.38 ± 0.08	-3.16 ± 0.08
O	$> 15.31 \pm 0.10$	$> -6.29 \pm 0.10$	$> -2.95 \pm 0.10$
Mg	$> 14.11 \pm 0.08$	$> -7.49 \pm 0.08$	$> -3.02 \pm 0.08$
Al	13.59 ± 0.10	-8.01 ± 0.10	-2.38 ± 0.10
Si	14.80 ± 0.08	-6.80 ± 0.08	-2.31 ± 0.08
S	14.89 ± 0.10	-6.71 ± 0.10	-1.85 ± 0.10
Ca	13.25 ± 0.08	-8.35 ± 0.08	-2.66 ± 0.08
Fe	14.86 ± 0.09	-6.74 ± 0.09	-2.19 ± 0.09
Ni	13.92 ± 0.13	-7.68 ± 0.13	-1.91 ± 0.13

4.3. Excited levels

The level structure of an atom or ion is characterized by a principal quantum number n , which defines the atomic level, and by the spin-orbit coupling (described by the quantum number j), which splits these levels into fine structure sub-levels. In GRB absorption spectra, several excited features are detected at the GRB redshift, due to the population of both $n > 1$ and/or $n = 1$

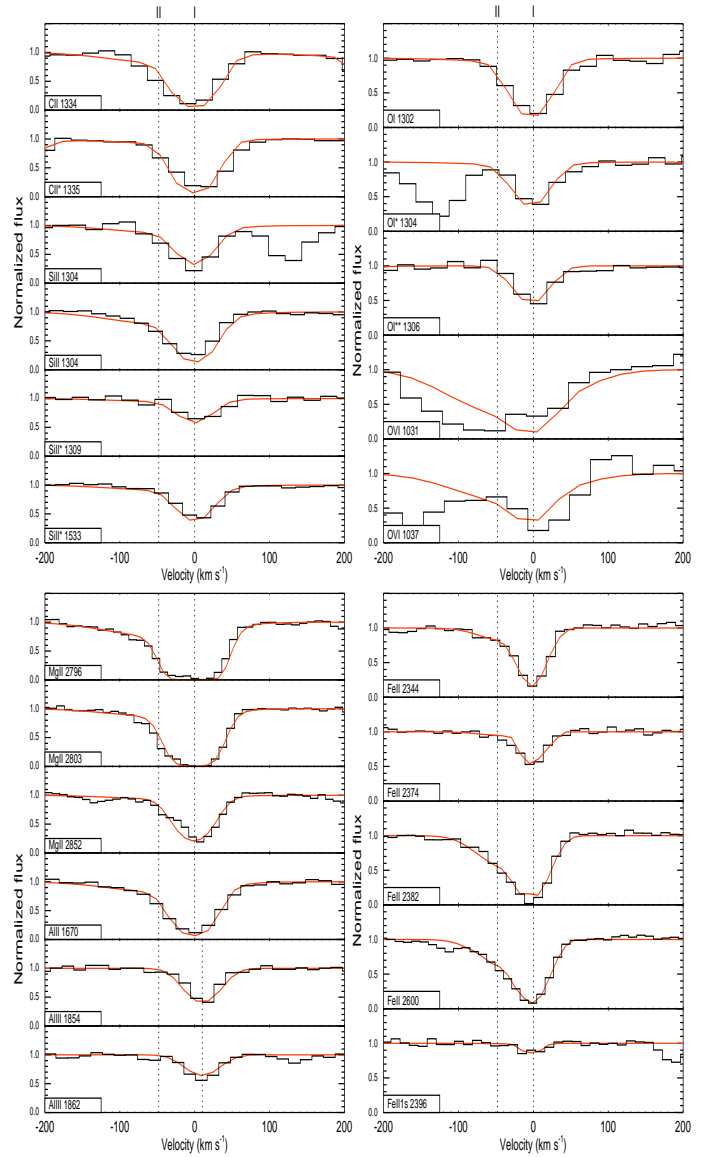


Fig. 3. The C II and Si II (top left panel), O I and O VI (top right panel), Mg I, Mg II, Al II and Al III (bottom left panel), Fe II (bottom right panel) absorption features. Solid lines represent the two Voigt components, best fit model. Vertical lines identify the component velocities. The zero point has been arbitrarily placed at the redshift of the red component ($z = 2.1071$). The O VI features are blended at blue wavelengths. Component I of Al III has been slightly shifted in order to be adequately fitted.

fine structure levels. As mentioned before, component I of the main system in the spectrum of GRB 090926A shows several absorptions from excited states. In particular, the first fine structure level of the Fe II ground state (a^6D), the Si II $^2P_{3/2}^0$, C II $^2P_{3/2}^0$, O I 3P_1 and O I 3P_0 fine structure levels and the Ni II $^4F_{9/2}$ metastable level are present. Moreover, excited states of Si II, C II and (marginally) Ni II are detected also in component II (see Table 2 for details).

There are basically two mechanisms to excite the gas of the GRB host galaxy to such states. The first is through collisional effects (if the electron density is sufficiently high, i.e., $\geq 10^5 \text{ cm}^{-3}$); the second is through the absorption of electromagnetic radiation. In the latter case, the absorbed photons can be infrared, through direct population of the fine-structure levels of

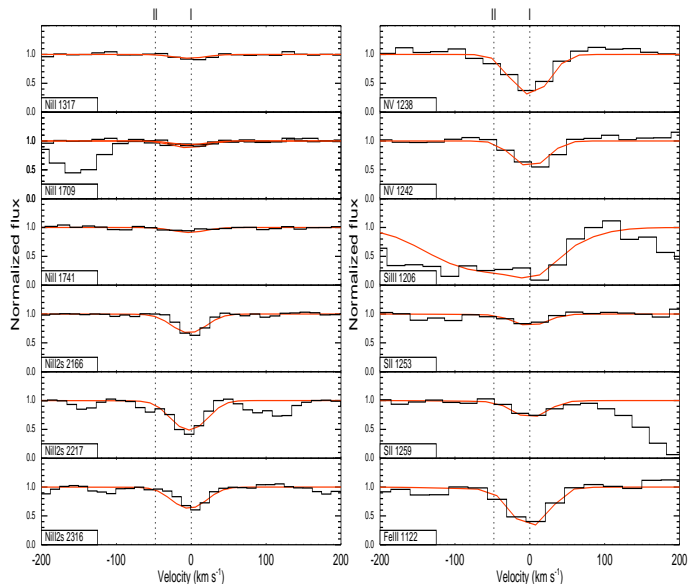


Fig. 4. Left panel: the Ni II absorption features. Right panel: the N V, Si III, S II and Fe III absorption features. Solid lines represent the two Voigt components, best fit model. Vertical lines identify the component velocities. The zero point has been arbitrarily placed at the redshift of the red component ($z = 2.1071$). The blue component of Si III is blended with absorption from the Ly α forest.

the ground state and other excited levels with a low value of n , or UV, through the population of higher levels followed by the de-population into the states responsible for the absorption features. Multi-epoch spectroscopy together with proper modeling of the atomic level population has proven to be a powerful tool to discriminate between these two processes. The strong variability in the column density of the Fe II and Ni II excited levels observed in GRB 060418 (Vreeswijk et al. 2007) and GRB 080319B (D’Elia et al. 2009a) ruled out collisional processes and direct infrared pumping as being responsible for the excitation. A collisional origin of the excitation can be ruled out even if multi-epoch spectroscopic data are missing. In fact, collisions populate higher energy levels less than lower energy ones. For instance, GRB 080330 (D’Elia et al. 2009b) and GRB 050730 (Ledoux et al. 2009) exhibit a Fe II $a^4F_{9/2}$ excited state column density larger than that of several fine structure levels of the Fe II a^6D ground state. This means that radiative processes are at work also for these GRBs. For GRB 090926A we do have multi-epoch spectroscopy, but the time lag between different observations (a few minutes, see Table 1) is too short when compared to the time delay between the GRB explosion and the epoch at which our data were taken. Supported by these results on atomic excitation mechanisms, we assume that indirect UV pumping by the fading afterglow is at work also for GRB 090926A.

As a first step, we assume a steady state flux coming from the GRB, which in general is not a good approximation. Nevertheless, the GRB 090926A afterglow was observed by X-shooter almost one day after the GRB explosion, and its flux level was decaying slowly at this stage. Under this assumption, we compute the ratio between the first excited level and the ground state for Si II, O I and Fe II. We then use these values as input for the plot in Fig. 7 of Prochaska, Chen & Bloom (2006) in order to estimate the flux experienced by the absorbing gas. This plot has been produced using the model from Silva

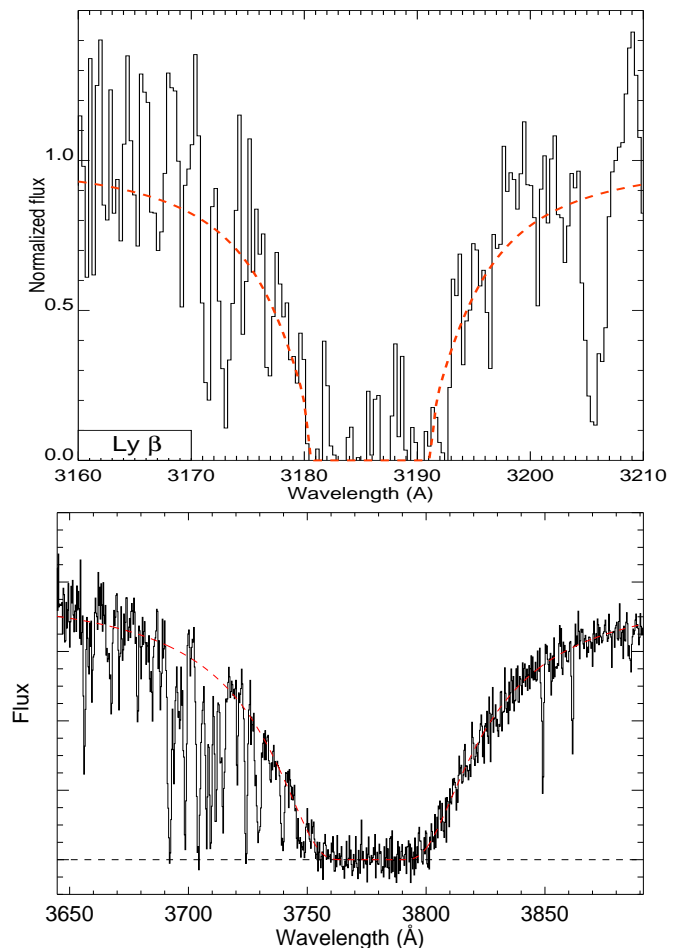


Fig. 5. The Ly β (top panel) and Ly α (bottom panel) absorption features at the GRB 090926A redshift. The dashed lines represent the single Voigt component, best fit model, centered at the redshift of the red component ($z = 2.1071$) of the metallic lines.

& Viegas (2002), which further assumes optically thin clouds. We first note that for component I the Fe II and Si II ratios are not compatible, i.e., the flux levels inferred from these ions are not consistent. This is possibly due to a slight saturation of the Si II $\lambda 1526$ line (see Fig. 3, top left), which was formerly used together with the $\lambda 1304$ transition to evaluate the Si II column density. Therefore, we recomputed the Si II column density using just the Si II $\lambda 1304$ line, as described in Sect. 4.1. The flux levels with the new $N_{\text{Si II}}$ for component I are now fully compatible. We further note that the O I ratio is far from being compatible with that of Si II and Fe II. This confirms the saturation of the O I $\lambda 1302$ transition (Fig. 3, middle), which can just be used to set a lower limit to the O I ground state column density. The Si II ratio for component II is close to that for I. Thus, we derive a distance of the gas responsible for the absorption of the two components I and II of $d = 1.8 \pm 0.2$ kpc.

To check the results from the steady state approximation, we must compare our observed column densities to those predicted by a photo-excitation code for the time when the spectroscopic observations have been acquired. The photo-excitation code is that used by Vreeswijk et al. (2007) and D’Elia et al. (2009), to which we refer the reader for further details. Basically, it solves the detailed balance equation in a time-dependent way for a set of transitions involving the levels of a given species (e.g. Fe II

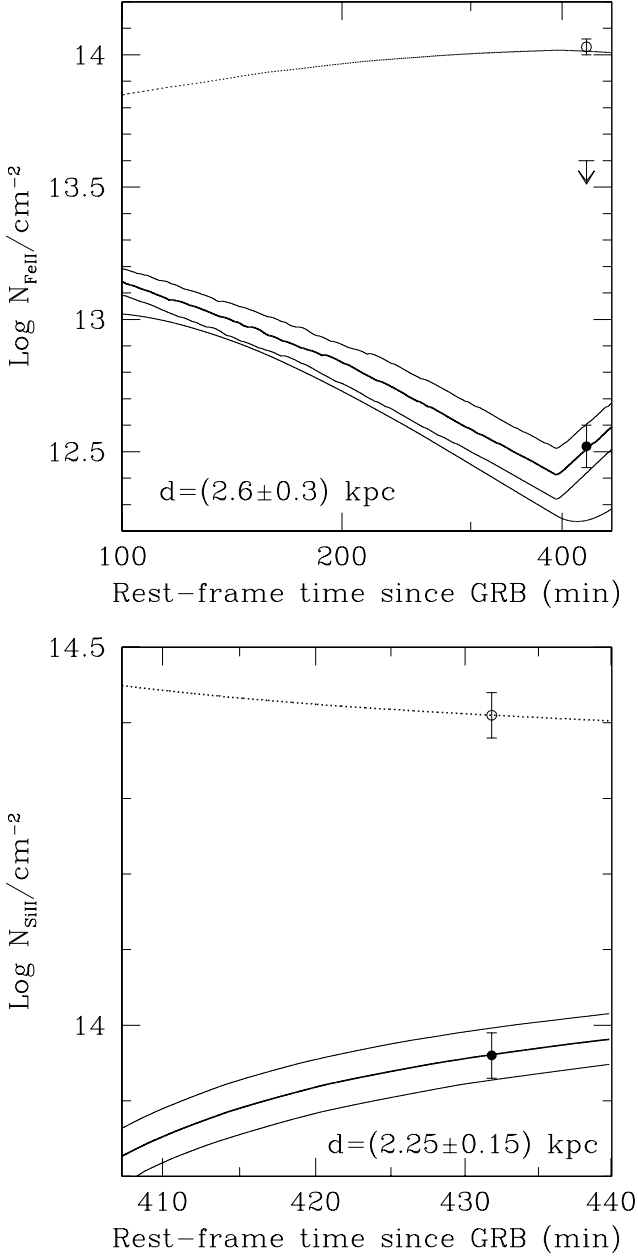


Fig. 6. Top panel: Fe II column densities for the ground level (open circle), first fine structure level (filled circle) and first excited level (upper limit) transitions for component I in the spectrum of GRB 090926A. Column density predictions from our time-dependent photo-excitation code are also shown. They refer to the ground level (dotted line), first fine structure level (thick solid line) and first excited level (dashed line) transitions, in the case of an absorber placed at 2.6 kpc from the GRB. The two thin solid lines display the models which enclose the fine structure data at 1σ level. Bottom panel: same as top panel, but for ground and first fine structure level transitions of Si II.

and Si II). The equation depends on the flux level experienced by the absorbing gas. This flux is of course a function of the distance d of the gas from the GRB explosion site, which is a free parameter of the computation and the quantity we want to calculate. The other free parameters are the initial column densities of the levels involved, which are assumed to be in the ground state

before the GRB flux reaches the gas, and the Doppler parameter of the gas itself. The afterglow spectral index has been calculated directly from the merged, flux-calibrated X-shooter spectrum, and is $\beta \sim 0.9$ (see Sect. 6). The flux behaviour before the X-shooter observation has been estimated using the data in R10. In detail, if the flux in the R band is $F_R = F_R(t_*) \times (t/t_*)^{-\alpha}$, we have $F_R(t_*) = 1.1 \times 10^{-27} \text{ erg cm}^{-2} \text{ s}^{-1} \text{ Hz}^{-1}$ at $t_* = 72.9 \text{ ks}$, with a decay index α of 1.6 (-2.7) before (after) t_* . No spectral variation is assumed during the time interval between the burst and our observation (this assumption is strongly supported by the R10 data). The initial column densities of the ground states have been computed from the observed column densities of all the levels of each ion. The exact values are: $\log(N_{\text{Si II}}/\text{cm}^{-2}) = 14.44 \pm 0.04$ and $\log(N_{\text{Fe II}}/\text{cm}^{-2}) = 14.04 \pm 0.03$. Finally, the Doppler parameter values used as input of this model are 30 and 90 km s^{-1} , i.e. the values that best fit the Fe II and Si II absorptions corresponding to components I and II, respectively.

We first modeled the Fe II photo-excitation. Fig. 6 (top) shows the model which best fits the Fe II data and the two theoretical curves compatible within the error bars for the first Fe II fine structure level column density. The distance of component I from the GRB explosion site results $d = 2.6 \pm 0.3 \text{ kpc}$. The same calculation has been performed using the Si II atomic data. The results are displayed in Fig. 6 (bottom), and the estimated distance is $d = 2.25 \pm 0.15 \text{ kpc}$, which is consistent with that estimated using the Fe II data. In addition, our distances are less than 30% away from that estimated using the code by Silva & Viegas (2002), and compatible with it at the 2σ level, confirming that the steady state and optically thin approximations are appropriate for component I of GRB 090926A. Regarding component II, we do not have Fe II excited features, so we can just set a lower limit to the GRB/absorber distance, which is 2.1 (2.2) kpc adopting a Doppler parameter of 30 (90) km s^{-1} . The Si II fine structure features are instead present in component II. The lack of Fe II excited levels in components featuring Si II fine structure ones is not atypical, see e.g. component III of GRB 050730 identified in D'Elia et al. (2007). Nevertheless, the large errors for this feature and the strong dependence of the model for this component quite uncertain. We run our code using the Doppler parameters that best fit Components I (30 km s^{-1}) and II (90 km s^{-1}). The distance of component II from the GRB is found to be $4.4 \pm 0.6 \text{ kpc}$ for $b = 30 \text{ km s}^{-1}$, and $5.8 \pm 0.8 \text{ kpc}$ for $b = 90 \text{ km s}^{-1}$. Despite these values are consistent with the lower limits estimated through Fe II data, we caution that a direct comparison to check the Si II distance is missing.

5. Other features at the host redshift

In this section we turn our attention to the search for galactic emission lines (Sect. 5.1) and absorption features not due to matter in the atomic gas phase. The latter can be produced by molecules (Sect. 5.2) or DIBs (Sect. 5.3).

5.1. Emission lines from the host galaxy

We searched for most of the stronger emission lines like $[\text{O II}] \lambda 3727$, $[\text{O III}] \lambda 5007$ and the Balmer lines from the host galaxy but found none. We did this by subtracting the spectral PSF. To derive upper limits for e.g., $H\alpha$, we then added artificial emission lines of increasing strength to the data, until the line was easily detectable. For $H\alpha$, which in this case is observed at $2 \mu\text{m}$, we find that an emission line of $9 \times 10^{-18} \text{ erg s}^{-1} \text{ cm}^{-2}$ with an intrinsic velocity width of 100 km

s^{-1} would have been detected (barring slit losses). This means that we would have detected emission lines from a host galaxy with a star formation rate $\gtrsim 2M_{\odot} \text{ yr}^{-1}$ (Kennicutt 1998). We also note that there is no Ly α emission in the trough of the DLA. The 5σ detection limit in a 6\AA wide extraction window is $3.0 \times 10^{-17} \text{ erg s}^{-1} \text{ cm}^{-2}$ corresponding to $\text{SFR} < 1M_{\odot} \text{ yr}^{-1}$. However, this limit is much more sensitive to uncertainties in radiative transfer of Ly α photons and to host galaxy dust extinction (see, e.g., Hayes et al. 2010). Although there is no evidence for dust extinction from the SED of the afterglow radiative transfer can still completely remove the Ly α emission from the line-of-sight (e.g., Atek et al. 2008). We note that many GRB host galaxies do have higher SFR than this limit (e.g., Christensen et al. 2004), and we therefore expect to be able to detect emission lines from many high- z GRB hosts using X-shooter in the future.

5.2. Molecular absorption features

Molecular gas is expected to be found in star-forming environments, but the search for its absorption features has often given negative results (see e.g. Tumlinson et al. 2007). Fynbo et al. (2006) interpreted an absorption feature of the GRB 060206 afterglow spectrum as a possible H₂ detection. Prochaska et al. (2009) and Sheffer et al. (2009) reported the presence of strong H₂ and CO absorption features in the spectrum of the GRB 080607 afterglow. These are the first (and by now unique) positive detections of molecules in GRB host galaxies. For GRB 090926A, we searched for the strongest features of the CO molecule, e.g., CO $\lambda\lambda 1510, 1478$ and 1447 , but we found no evidence of absorption at these wavelengths. Quantitatively, the upper limit for the CO column density depends on the adopted Doppler value b . Assuming it is in the range $30 - 90 \text{ km s}^{-1}$ (i.e., the values that best fits components I and II, respectively, see Sect. 4.1), the resulting upper limit for the CO column density lies in the interval $\log(N_{\text{CO}}/\text{cm}^{-2}) < 14 - 14.3$. We also searched for H₂ absorption. The strongest H₂ transitions of the Lyman-Werner bands have a wavelength $< 3000 \text{\AA}$ at the redshift of GRB 090926A. Nevertheless, using the H₂ L2R0 transition, which falls around 3350\AA , we can set a 90% upper limit of $\log(N_{\text{H}_2}/\text{cm}^{-2}) < 14.9$ for a b parameter fixed at 30 km s^{-1} and $\log(N_{\text{H}_2}/\text{cm}^{-2}) < 15.3$ for b fixed at 90 km s^{-1} . Finally, we searched for other absorptions, due to the CH, CH⁺ and CN molecules, but also in these cases we found none.

5.3. Diffuse interstellar bands

DIBs (see Jenniskens & Desert 1994 and references therein) are broad absorption features in the near-infrared to UV wavelength range. They were observed for the first time more than 70 years ago in the Milky Way (Merrill 1934), and more recently in near galaxies (see e.g., Cox & Cordiner 2008, Cordiner et al. 2008). Although they have been known for a long time and hundreds of features have already been identified, the nature of the carrier of such transitions is still uncertain. The identification is difficult since most of them are not correlated with each other. The most promising candidates are large molecules, which are thought to be polycyclic aromatic hydrocarbons. We searched for the ten strongest and most common DIBs in the GRB 090926A afterglow spectrum, in the rest-frame wavelength range $\lambda = 4000 - 7000 \text{\AA}$, but we found no positive detection. A conservative 2σ upper limit to the rest frame equivalent width of these systems (taking into account that they have very different FWHM) is $\text{EW} < 0.3 \text{\AA}$. This limit is set by the signal-to-noise

ratio of the infrared arm of our X-shooter spectrum, i.e., is the “noise EW”.

6. The extinction curve shape

The shape of extinction curves at high redshift is a powerful tool to derive information about dust formation and possibly about the various processes affecting dust absorption and destruction close to GRB sites. In most cases, inferences about dust extinction curves are obtained by photometric observations of GRB afterglows which unfortunately is biased by a strong degeneracy between afterglow spectral slope and extinction. Moreover, in particular for very high redshift events, uncertainties in photometry of single bands which can also present specific calibration problems may affect the whole analysis (see for instance discussion in Stratta et al. 2007 and Zafar et al. 2010 about GRB 050904). For early time afterglows even the possible non-absolute simultaneity of the available photometric information has to be properly considered to avoid spurious results.

For most GRB afterglows, when accurate multi-band photometry is available (e.g., Covino et al. 2008, Schady et al. 2010, Kann et al. 2010), the derived extinction curve is in fair agreement with what observed locally in the Small Magellanic Cloud (SMC, Pei 1992) although often, due to the limited wavelength resolution, this simply means that the observed extinction curve has to be chromatic (i.e. wavelength dependent) and featureless. A few remarkable exceptions have been recorded in an intervening system along the line of sight of GRB 060418 (Vreeswijk et al. 2007), for GRB 070802 (Krühler et al. 2008; Elíasdóttir et al. 2009) and GRB 080607 (Prochaska et al. 2009), where the characteristic absorption feature at about 2175\AA , prominent in the Milky Way extinction curve, has also been detected.

Clearly, when spectroscopic information is available (e.g., Liang & Li 2010), better constrained results can be derived, disentangling the extinction curve and spectral slope effects.

The case of GRB 090926A is a good example of the X-shooter capabilities in this context. The flux calibrated spectrum (Fig. 1) has been analyzed after removing wavelength intervals affected by telluric lines of strong absorptions. The Ly α range has been included in the analysis due to the importance of its wavelength range for extinction determination using the Hydrogen column density reported in Table 2. We then rebin the spectrum in bins of approximately 50\AA by a sigma-clipping algorithm to avoid the effect of residuals absorption systems. The flux-calibration of X-shooter spectra ranging from the UV to the K band is not an easy task and the reduction pipeline (Goldoni et al. 2006) is still under active development. In order to obtain an acceptable fit we had to introduce additional systematic uncertainties at about $\sim 2.5\%$ level added in quadrature, which possibly reflects normalization biases of the three arms and/or still not fully modeled slit losses along the whole wavelength range. Assuming a power-law spectrum, we obtained $\beta = 0.89 \pm 0.02$ (errors at 1σ) where the afterglow spectrum is modeled, as customary in GRB literature, as $F_{\nu} \propto \nu^{-\beta}$. We try to fit the data using different extinction curves, namely, SMC, LMC, Milky Way and Starburst. The best fit is obtained assuming a SMC extinction curve with $E_{B-V} < 0.01 \text{ mag}$ at 3σ ($\chi^2/\text{dof} = 1.14$ for 484 dof). Other extinction curve recipes were not required by the data.

7. The GRB 090926A line of sight

The absorption lines due to the gas belonging to the GRB host galaxy are the dominant features of our spectrum, but they are

not the only ones. A detailed analysis of the data reveals that at least four other absorbers are present along the line of sight to GRB 090926A. Three of these systems, those with the highest redshifts ($z = 1.75 - 1.95$), show absorption from the CIV $\lambda\lambda 1548, 1550$ doublet, to which corresponds a well defined HI $\lambda 1215$ line inside the Ly α forest. All these systems exhibit a very simple line profile, that can be fitted by a single Voigt function (Fig. 7). The Ly α of the system at $z = 1.7986$ requires a Doppler parameter that is about three times that for the CIV doublet, in order to be adequately fit. Anyway, if we assume a double component model for this Lyman- α feature, and fix the b parameter of one component to that of the CIV doublet, the estimated N_{H} column density is not significantly different from that computed using the single component model. The last of the GRB 090926A intervening systems has a lower redshift ($z = 1.2456$) and features absorption from the Mg II $\lambda\lambda 2796, 2803$ doublet and marginally (2.7σ) from the Mg I $\lambda 2852$ line. This is a rather weak system, and the rest frame equivalent width for the Mg II $\lambda 2796$ line is just $\text{EW}_r = 0.19 \pm 0.06 \text{ \AA}$ (2σ confidence). Again, a single component Voigt profile describes well the absorption features (Fig. 7).

Table 4 summarizes the rest frame equivalent widths, column densities and redshifts calculated for these intervening systems.

Table 4. Redshifts, absorption line column densities and equivalent widths for the intervening systems.

	Species	Transition	Redshift	$\log(N/\text{cm}^{-2})$	$\text{EW}_r (\text{\AA})^a$
1	CIV	1548, 1550	1.9466	13.70 ± 0.03	0.15 ± 0.04
1	HI	Ly α	1.9466	14.64 ± 0.04	
2	CIV	1548, 1550	1.7986	13.63 ± 0.03	0.11 ± 0.03
2	HI	Ly α	1.7986	14.56 ± 0.07	
3	CIV	1548, 1550	1.7483	13.90 ± 0.02	0.21 ± 0.03
3	HI	Ly α	1.7483	14.98 ± 0.41	
4	MgII	2796, 2803	1.2456	12.39 ± 0.05	0.19 ± 0.06
4	MgI	2852	1.2456	11.47 ± 0.13	

^a Rest frame equivalent widths for Mg II $\lambda 2796$ and CIV $\lambda 1548$; EW errors are given at the 2σ confidence level.

8. Conclusions and discussion

In this paper we present intermediate resolution ($R = 10,000$) spectroscopy of the optical afterglow of GRB 090926A, observed using the X-shooter spectrograph at the VLT ~ 22 hr after the trigger.

From the detection of Hydrogen and metal absorption features, we find that the heliocentric redshift of the host galaxy is $z = 2.1071$. The spectrum shows that the ISM of the GRB host galaxy has at least two components contributing to this main absorption system at $z = 2.1071$. Such components, whose line centres are separated by $\sim 48 \text{ km s}^{-1}$, are identified in this paper as I and II, according to their decreasing velocity values. The total width of the two components is $\sim 250 \text{ km s}^{-1}$. We stress that the identification of just two components may be due to the X-shooter resolution. In fact, GRB afterglows observed with higher spectral resolution feature more complex environments either if the host galaxy absorber has a similar width (e.g., 7 components for GRB 050922C, see Piranomonte et al. 2008) or even in case of smaller widths (GRB 080319B has six components for a total width of $\sim 120 \text{ km s}^{-1}$, see D’Elia et al. 2009a).

The absorption lines appear both as neutral metal-absorption, low ionization and high ionization species. In addition, strong

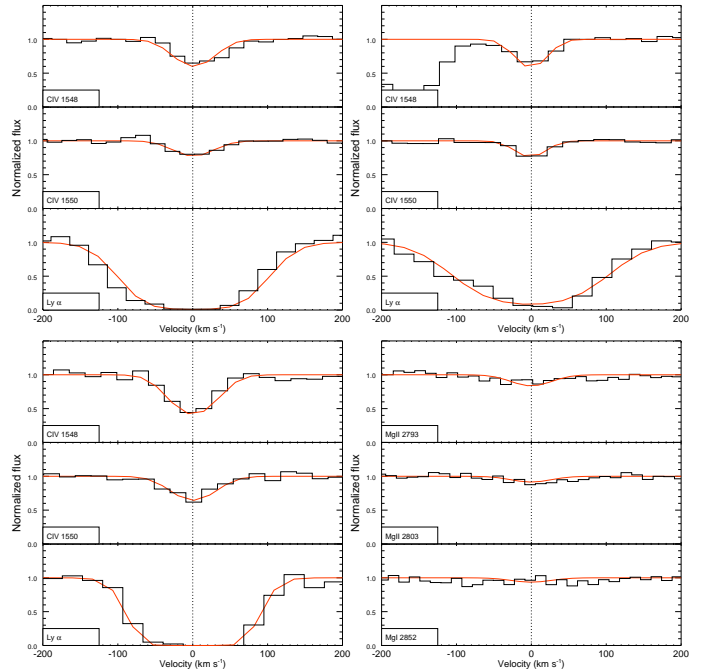


Fig. 7. The four intervening systems along the GRB090926A sightline. Top left: intervening 1 at $z = 1.9466$; top right: intervening 2 at $z = 1.7986$; bottom left: intervening 3 at $z = 1.7483$; bottom right: intervening 4 at $z = 1.2456$. The first three systems feature the CIV doublet and Ly α . System 4 shows Mg I and Mg II, with the $\lambda 2852$ transition and $\lambda 2796 - \lambda 2803$ doublet, respectively. Mg I is marginally detected (2.7σ). Solid lines represent our best fit model (see also Table 4).

absorption from the fine structure and metastable levels of several species are detected. The distances between the GRB and the two absorbers have been estimated using the code by Silva & Viegas (2002), in a steady state and optically thin approximation, using the ratios between the ground state and the first excited levels of different species to infer the flux level experienced by the absorbing gas. For both components we find that the absorber is located at a distance of $d = 1.8 \pm 0.2 \text{ kpc}$.

The value of this distance can be refined by comparing the column densities of the ground and excited levels to those predicted by a time dependent photo-excitation code. Using Fe II and Si II we find that the absorbing gas of component I is located at $d = 2.40 \pm 0.15 \text{ kpc}$ from the GRB, a value which is in not far from that estimated assuming a steady state approximation. For component II, this distance is larger, $\sim 5 \text{ kpc}$, but this value has been obtained using Si II only, because we just have a lower limit for the Fe II fine structure column density. Despite this lower limit gives a distance consistent to the Si II result, a safe cross check can not be performed.

The GRB 090926A/absorber distance is compatible with that found for the 4 other GRBs for which a similar analysis has been performed, i.e., 1.7 kpc for GRB 060418 (Vreeswijk et al. 2007), 2 – 6 kpc for GRB 080319B (D’Elia et al. 2009a), 280 pc for GRB 080330 (D’Elia et al. 2009b) and 440 pc for GRB 050730 (Ledoux et al. 2009). This is a further confirmation that the power of a GRB affects a region of gas which is at least a few hundreds pc in size.

Several high ionization lines are detected in the GRB090926A spectrum (see Table 2). Our NV column density is within the range of the GRB sample studied by Prochaska et al. (2008), who claim that this ion can be located

very close to the GRB explosion site. Fox et al. (2008) estimated a lower limit to the S IV distance from the absorber using the non detection of the S IV fine structure feature and a photoexcitation code similar to that used in this paper. They conclude that for GRB 050730 this ion is located at distances greater than 400 pc. An upper limit of the same order of magnitude can be roughly estimated also for GRB090926A, since we compute a tighter limit for the S IV* column density of $\log(N_{\text{SIV}}/\text{cm}^{-2}) < 13.3$, but the flux of our GRB is about three times smaller than that of GRB 050730 (compared at the time of the acquisition of the spectra). In addition, Fox et al. (2008) report the detection in six of the seven GRB spectra analyzed in their work of CIV high velocity components at 500-5000km/s. These gas can belong to foreground clouds but also be associated to the Wolf-Rayet wind of the GRB progenitors. We do not find any of such absorptions in the spectra of GRB 090926A.

The redshift of GRB 090926A allows us to determine the Hydrogen column density, which has $\log(N_{\text{H}}/\text{cm}^{-2}) = 21.60 \pm 0.07$. This value is lower than that found by R10 ($\log(N_{\text{H}}/\text{cm}^{-2}) = 21.79 \pm 0.07$), but the 2σ regions overlap, and each value is consistent with the other at the 2.7σ level. Using N_{H} we evaluate the GRB 090926A host galaxies metallicity. The values we find are in the range $10^{-3} - 10^{-2}$ with respect to the solar abundances (see Table 3). R10 report a metallicity calculated using S II, Si II, Al II, O I and Fe II. The first three values are in perfect agreement with our estimates for S, Si and Al. Their O I value is consistent with our Oxygen lower limit (set mainly by the saturated O I features). However, the authors note that their extremely low value (~ -3.08) is possibly due to saturation and it could consequently lead to an underestimate of the O I column density, and thus this should be regarded as a lower limit as well. Another way to derive a metallicity using Oxygen, is to evaluate the O I ground state column density through the fine structure one, in the hypothesis of a steady state UV pumping as the responsible for this excitation. This has proven to be a good approximation for component I, the only one featuring O I. Under this assumption, we obtain $\log(N_{\text{OI}}/\text{cm}^{-2}) \sim 16.05$ and a metallicity of $[\text{O}/\text{H}] = -2.18 \pm 0.16$, which is consistent with the values obtained using other elements. Finally, the R10 metallicity obtained using the Fe II features ($[\text{Fe}/\text{H}] \sim -2.93$) is not consistent with our Iron value of $[\text{Fe}/\text{H}] = -2.19 \pm 0.07$. This is because we considered the Fe III $\lambda 1122$ line which brings a relevant contribution to the total Iron column density for GRB 090926A. Due to this contribution, we do not detect an overabundance of Silicon with respect to Iron, contrary to what reported by R10.

For what concerns our results, the extremely low value derived for N ($[\text{N}/\text{H}] \sim -3.31$) is most certainly due to the fact that we could not fit low ionization lines, but the NV species only. For Ca ($[\text{Ca}/\text{H}] \sim -2.71$) we can not exclude a possible contamination by sky lines. Despite this, we still have a metallicity in the range $4.2 \times 10^{-3} - 1.4 \times 10^{-2}$ with respect to solar. The average, logarithmic metallicity is $[\text{X}/\text{H}] = -2.14 \pm 0.09$ and is consistent with that computed by the R10 data excluding Oxygen and Iron. This value lies at the lower end of the GRB distribution (Savaglio 2006, Prochaska et al. 2007, Savaglio, Glazebrook & Le Borgne, 2009), in fact, only GRB 050730 and GRB 050922C have metallicity values below 10^{-2} .

A powerful way to infer the nature and the age of objects whose morphology is unknown is to use abundances and abundance ratios (see Matteucci 2001). This method is based on the fact that galaxies of different morphological type are characterized by different star formation histories and these strongly influence the $[\text{X}/\text{Fe}]$ versus $[\text{Fe}/\text{H}]$ behaviour. For very large star formation rates, as expected in spheroids (bulges and ellipticals)

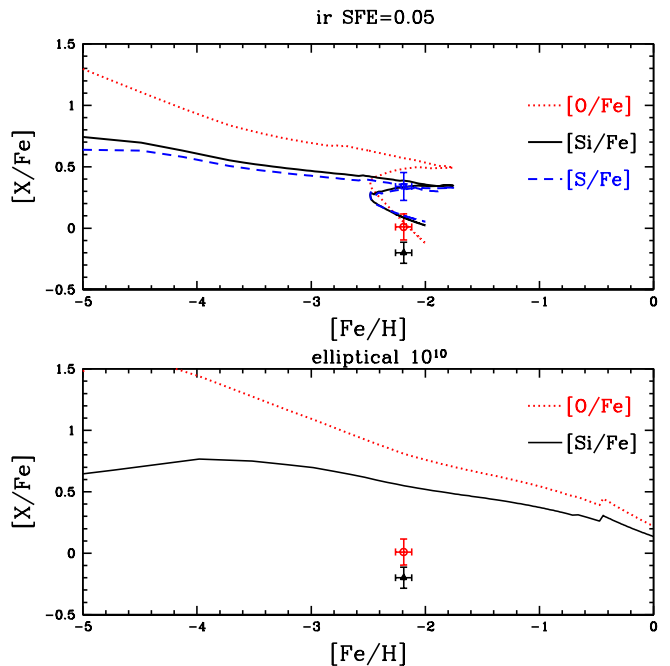


Fig. 8. Predicted $[\text{X}/\text{Fe}]$ vs. $[\text{Fe}/\text{H}]$ for a typical irregular galaxy (upper panel) with a baryonic mass of $10^8 M_{\odot}$ (star formation efficiency of 0.05 Gyr^{-1}) and for a small elliptical with baryonic mass $M = 10^{10} M_{\odot}$ (lower panel). The data for GRB 090926A are shown for comparison.

in their evolution phases, the $[\alpha/\text{Fe}]$ ratios are overabundant relative to the Sun in a large range of $[\text{Fe}/\text{H}]$ values, and this is because in a regime of strong star formation the large number of Type II SNe acting in the early phases of galaxy evolution increases the $[\text{Fe}/\text{H}]$ in the gas up to large values (almost solar and solar) on timescales too short for the Type Ia SNe to substantially enrich the gas in Fe. Therefore, the $[\alpha/\text{Fe}]$ ratios will reflect the production ratio of SNe II which is larger than in the Solar birthplace. In fact, the bulk of Fe is supposed to have been produced by Type Ia SNe. On the other hand, objects evolving slowly with a low star formation rate, with respect to normal ellipticals, such as irregular galaxies, would show low $[\alpha/\text{Fe}]$ ratios even at low $[\text{Fe}/\text{H}]$ values. This is because in this case SNe Ia have time to pollute the gas much before it reaches the Fe solar value. Therefore, if we compare the measured abundance ratios in the host of GRB 090926A with predictions from detailed chemical evolution models we can in principle understand the nature of the host. This is done in Fig. 8 where models for ellipticals and for irregular galaxies are compared with the measured abundances. These models, which are discussed in Fan et al. (2010, in preparation), show that the host of GRB 090926A is probably an irregular galaxy with baryonic mass $10^8 M_{\odot}$ and evolving with a star formation efficiency (the inverse of the timescale of star formation) of 0.05 Gyr^{-1} . In fact the measured $[\alpha/\text{Fe}]$ ratios agree better with the prediction for the irregular and are instead too low for an elliptical galaxy of baryonic mass $10^{10} M_{\odot}$, shown for comparison. The model for the irregular galaxy takes into account metal-enhanced galactic winds, induced by SN feedback, which produce the loops in the predicted abundance ratios.

This kind of host galaxy, associated with the low metallicity of the GRB 090926A ISM, agrees with the tentative evidence for a trend of declining ISM metallicity with decreasing galaxy

luminosity in the star-forming galaxy population at $z = 2 - 4$ (Chen et al. 2009).

We also searched for other features at the host galaxy redshift. No emission lines were detected for the GRB 090926A host, but our lower limits ensure that we will be able to detect emission lines from many high-redshift GRB hosts using X-shooter in the future. Similarly, we find no evidence for molecular absorption at the GRB redshift. The lower limit on H_2 translates into an upper limit for the Hydrogen molecular fraction of $f = 2N_{H_2}/(2N_{H_2} + N_H) < (3.0 - 7.4) \times 10^{-7}$. The absence of molecules is not surprising, since Hydrogen molecular fractions $\log f > -4.5$ are detected in just 10% of the QSO-DLA population. In addition, GRB environments with metallicities below $0.1Z_\odot$ (such as that of GRB 090926A) and low dust content can explain the lack of H_2 (see Ledoux et al. 2009). As a confirmation of this scenario, the only positive detection of molecules in GRB host galaxies has been reported in the GRB 080607 afterglow, for which a solar or even super-solar metallicity has been inferred (Prochaska et al. 2009). Finally, DIBs have not been detected either.

The GRB 090926A continuum has been fitted assuming a power-law spectrum. The best fit spectral index is $\beta = 0.89^{+0.02}_{-0.02}$ (1σ). This value is consistent with that obtained in R10 by fitting the GROND data ($0.98^{+0.06}_{-0.07}$), and is close to that obtained by the same authors fitting the optical/IR and the X-ray data together (~ 1.03). Our best fit does not essentially allow for any intrinsic extinction since $E_{B-V} < 0.01$ mag at 3σ adopting an SMC extinction curve. Other extinction curve recipes are not required by the data. This intrinsic extinction limit is consistent with that reported by R10.

The GRB 090926A sightline has also been analyzed. The signal-to-noise level of our spectrum allowed us to be sensitive to lines with equivalent width (observed frame) as weak as $0.06 - 0.15 \text{ \AA}$ (depending on the spectral region), at the 2σ confidence level. The redshift path analyzed for the search of Mg II (CIV) systems ranges from $z = 2.107$ to $z = 0.35$ ($z = 1.44$). Four intervening systems between $z = 1.95$ and $z = 1.24$ have been identified. All systems have rest frame equivalent widths very small, below 0.3 \AA . Two of these systems, those marked as 1 and 3 in Table 4, have also been reported by R10, and their equivalent widths are consistent with ours. The line of sight toward GRB 090926A is thus very clean, if compared to that of other GRBs. In fact, Prochter et al. (2006) and Vergani et al. (2009) claimed an excess of strong ($EW > 1 \text{ \AA}$) Mg II absorbers along GRB sight lines with respect to QSO's. On the other hand, the number of CIV and weak Mg II systems is consistent along the line of sight of the two classes of objects (Tejos et al. 2007, 2009). The reason for the strong Mg II discrepancy is still uncertain, despite several possibilities have been already ruled out (e.g. Porciani et al. 2007, D'Elia et al. 2010). The only proposed explanation which is still a possible candidate for this discrepancy is a multiband magnification bias in GRB sightlines (Vergani et al. 2009). Anyway, more observations and analysis are needed in order to solve this issue.

Acknowledgements. We thank an anonymous referee for several helpful comments in improving the quality and clarity of the paper. The Dark Cosmology Centre is funded by the Danish National Research Foundation.

References

- Asplund, M., Grevesse, N.; Sauval, A.J. & Scott, P. 2009, *ARA&A*, 47, 481
 Atek, H., Kunth, D., Hayes, M., Östlin, G. & Mas-Hesse, J.M. 2008, *A&A*, 482, 491
 Bissaldi, E. 2009, *GCN Circ*, 9933

- Bohlin, R.C. 2004, in *Astronomical Society of the Pacific Conference Series*, 364, 315
 Bohlin, R.C. & Gilliland, R.L. 2004, *AJ*, 128, 3053
 Chen, H.W., Perley, D.A., Pollack, L.K. et al. 2009, *ApJ*, 691, 152
 Christensen, L., Hjorth, J. & Gorosabel, J. 2004, *A&A*, 425, 913
 Cordiner, M.A., Smith, K.T., Cox, N.L.J., Evans, C.J., Hunter, I., Przybilla, N., Bresolin, F. & Sarre, P.J. 2008, *A&A*, 492, 5L
 Covino, S., D'Avanzo, P., Klotz, A., et al. 2008, *MNRAS*, 388, 347
 Cox, N.L.J. & Cordiner, M.A. 2008, *IAUS*, 251, 237
 Cucchiara, A., Jones, T., Chertlton, J.C., Fox, D.B., Einsig, D., Narayanan, A. *ApJ*, 693, 345
 D'Elia, V., Fiore, F., Perna, R. et al. 2009a, *ApJ*, 694, 332
 D'Elia, V., Fiore, F., Perna, R. et al. 2009b, *A&A* 503, 437
 D'Elia, V., Fiore, F., Goldoni, P. et al. 2010, *MNRAS* 401, 385
 de Ugarte Postigo, A., Goldoni, P., Thöne, C.C. et al. 2010, *A&A*, 513, 42
 D'Odorico, S., Dekker, H., Mazzoleni, R. et al. 2006, in *SPIE Conf. Series*, Vol. 6269
 Elíasdóttir, Á., Fynbo, J.P.U., Hjorth, J., et al. 2009, *ApJ*, 697, 1725
 Fan et al. 2010, in preparation
 Fiore, F.; D'Elia, V.; Lazzati, D. et al. 2005, *ApJ*, 624, 853
 Fontana, A. & Ballester, P. 1995, *The Messenger*, 80, 37
 Fox, A.J., Ledoux, C., Vreeswijk, P.M., Smette, A. & Jaunsen, A.O. 2008, *A&A*, 491, 189
 Fynbo, J.P.U., Starling, R.L., Ledoux, C. et al. 2006, *A&A* 451 L47
 Fynbo, J.P.U., Prochaska, J.X., Sommer-Larsen, J.; Dessauges-Zavadsky, M. & Moller, P. 2008, *ApJ*, 683, 321
 Goldoni, P., Royer, F., Francois, P. et al. 2006, in *Society of Photo-Optical Instrumentation Engineers (SPIE) Conference Series*, Vol. 6269
 Gronwall, C. and Vetere, L. 2009, *GCN Circ* 9938
 Haislip, J. et al. 2009, *GCN Circ* 9937
 Hayes, M., Östlin, G., Schaerer, D. et al. 2010, *Nature*, 464, 562
 Jenniskens, P. & Desert, F.-X. 1994, *A&AS*, 39, 206
 Kann, D.A., Klose, S., Zhang, B. et al. 2010, submitted, arXiv:0804.1959
 Kelson, D.D. 2003, *PASP*, 115, 688
 Kennicutt, R.C. 1998, *ApJ*, 498, 541
 Krühler, T., Küpcü Yıldız, A., Greiner, J., et al. 2008, *ApJ*, 685, 376
 Ledoux, C., Vreeswijk, P.M., Smette, A. et al. 2009, *A&A*, 506, 661
 Liang, S.L., & Li, A. 2010, *ApJ*, 710, 1
 Malesani, D. et al. 2009, *GCN Circ* 9942
 Matteucci, F. 2001, *AASL*, Kluwer Academic Publisher
 Merrill, P.W. 1934, *PASP*, 46, 206
 Oates, S.R. 2010, *GCN* 9948
 Pei, Y.C. 1992, *ApJ*, 395, 130
 Piranomonte, S., Ward, P.A., Fiore, F. et al. 2008, *A&A*, 492, 775
 Porciani, C., Viel, M. & Lilly, S.J. 2007, *ApJ*, 659, 218
 Prochaska, J.X., Chen, H.W., Bloom, J.S. 2006, *ApJ*, 648, 95
 Prochaska J.X., Chen, H.W., Dessauges-Zavadsky, E. & Bloom, J.S. 2007, *ApJ*, 666, 267
 Prochaska J.X., Dessauges-Zavadsky M., Ramirez-Ruiz M. & Chen, H.W. 2008, *ApJ*, 685, 344
 Prochaska J.X., Sheffer, Y., Perley, D.A. et al. 2009, *ApJ*, 691, 27L
 Prochter, G.E., Prochaska, J.X., Chen, H.-W. et al. 2006, *ApJ*, 648, L930
 Rau, A., Savaglio, S., Krühler, T. et al. 2010, *ApJ* submitted, arXiv:1004.3261 (R10)
 Savaglio, S., Glazebrook, K., Crampton, D. et al. 2004, *ApJ*, 602, 51
 Savaglio, S., Glazebrook, K., Le Borgne, D. et al. 2005, *ApJ*, 635, 260
 Savaglio, S. 2006, *New J. Phys.*, 8, 195
 Savaglio, S., Glazebrook, K. & Le Borgne, D. 2009, *ApJ*, 691, 182
 Sheffer, Y., Prochaska, J.X., Draine, B.T., Perley, D.A. & Bloom, J.S. 2009, *ApJ*, 701, L63
 Silva, A.I. & Viegas, S.M., 2002, *MNRAS*, 329, 135
 Schady, P., Page, M.J., Oates, et al. 2010, *MNRAS*, 401, 2773
 Stratta, G., Maiolino, R., Fiore, F., & D'Elia, V. 2007, *ApJ*, 661, 9
 Sudilovsky et al. 2007, *ApJ*, 669, 741
 Tayyba, Z., Watson, D.J., Malesani, D., et al. 2010, *astro-ph/1002.4101*
 Tejos, N., Lopez, S., Prochaska, J.X., Chen, H.-W. & Dessauges-Zavadsky, M. 2007, *ApJ*, 671, 622
 Tejos, N., Lopez, S., Prochaska, J.X., Bloom, J.S., Chen, H.-W., Dessauges-Zavadsky, M.; Maureira, M.J. 2009, *ApJ*, 706, 1309
 Thone, C.C., Wiersema, K., Ledoux, C. et al. 2008, *A&A*, 489, 37
 Tumlinson, J., Prochaska, J.X., Chen, H.-W., Dessauges-Zavadsky, M. & Bloom, J.S. 2007, *ApJ*, 668, 667
 Uehara, T., Takahashi, H. and McEnery, J. 2009, *GCN Circ*, 9934
 van Dokkum, P.G. 2001, *PASP*, 113, 1420
 Vergani, S.D., Petitjean, P., Ledoux, C., Vreeswijk, P.M., Smette, A., Meurs, E.J.A. 2009, *A&A*, 503, 771
 Vetere, L., Evans, P.A., and Goad, M.R. 2009, *GCN Circ*, 9936
 Vetere, L. et al. 2010, *GCN* 9961

Vreeswijk, P.M., Ellison, S.L., Ledoux, C. et al. 2004, *A&A*, 419, 927
Vreeswijk, P.M., Ledoux, C., Smette, A. et al. 2007, *A&A*, 468, 83